HST/NICMOS Observations of NGC 1333: The Ratio of Stars to Sub-stellar Objects

Julia Greissl

Steward Observatory, University of Arizona, Tucson, AZ 85721

jgreissl@as.arizona.edu

Michael R. Meyer

Steward Observatory, University of Arizona, Tucson, AZ 85721

mmeyer@as.arizona.edu

Bruce A. Wilking

Department of Physics and Astronomy, University of St.Louis
1 University Blvd., St. Louis, MO 63121

Tina Fanetti

Department of Physics and Astronomy, University of St.Louis
1 University Blvd., St. Louis, MO 63121

Glenn Schneider

Steward Observatory, University of Arizona, Tucson, AZ 85721

Thomas P. Greene

NASA AMES Research Center, Moffet Field, CA 94035

Erick Young

Steward Observatory, University of Arizona, Tucson, AZ 85721

ABSTRACT

We present an analysis of NICMOS photometry and low-resolution grism spectroscopy of low-mass stars and sub-stellar objects in the young star-forming region NGC 1333. Our goal is to constrain the ratio of low-mass stars to sub-stellar objects down to 20 M_{Jup} in the cluster as well as constrain the cluster

IMF down to 30 M_{Jup} in combination with a previous survey of NGC 1333 by Wilking et al. Our survey covers 4 fields of 51.2" x 51.2", centered on brown dwarf candidates previously identified in Wilking et al. We extend previous work based on the use of a water vapor index for spectral typing to wavelengths accessible with NICMOS on the HST. Spectral types were derived for the 14 brightest objects in our fields, ranging from ≤M0 - M8, which at the age of the cluster (0.3 Myr) corresponds to a range in mass of ≥0.25 - 0.02 $M_{\odot}$. In addition to the spectra, we present an analysis of the color-magnitude diagram using pre-main sequence evolutionary models of D'Antona & Mazzitelli. Using an extinction-limited sample, we derive the ratio of low-mass stars to brown dwarfs. Comparisons of the observed ratio to that expected from the field IMF of Chabrier indicate that the two results are consistent. We combine our data with that of Wilking et al. to compute the ratio of intermediate-mass stars (0.1 - 1.0 $M_{\odot}$) to low-mass objects (0.03 - 0.1 $M_{\odot}$) in the cluster. We also report the discovery of a faint companion to the previously confirmed brown dwarf ASR 28, as well as a possible outflow surrounding ASR 16. If the faint companion is confirmed as a cluster member, it would have a mass of ≈ 5 M_{Jup} (mass ratio 0.15) at a projected distance of 350 AU, similar to 2MASS 1207-3923 B.

Subject headings: stars: pre-main-sequence, brown dwarfs – stars: mass function – stars: formation – infrared: stars – ISM: individual (NGC 1333)

1. Introduction

The shape of the Initial Mass Function (IMF) and its connection to the initial physical conditions in molecular clouds remains one of the fundamental questions in star formation. More specifically: Does the young cluster IMF mimic the integrated field star IMF even to very low masses? Is there a low-mass cut-off to the sub-stellar mass function?

The IMF over the full range of stellar masses has been extensively studied in the past decades starting with Miller & Scalo (1979), as well as updates by Kroupa et al. (1993) and Chabrier (2003). It is generally accepted that young clusters exhibit a Salpeter-like IMF above 1 $M_{\odot}$, flattening out towards low-mass stars. Studies of the IMF have been concentrated on young clusters, because they offer several beneficial characteristics. Their populations are less likely to have undergone significant dynamical mass segregation compared to older clusters, which means that a small field can yield a sample representative of the whole cluster. In addition, young low mass stars are still located significantly above the main sequence and are thus several times brighter than their main sequence counter-

parts. Lastly, young clusters are fairly compact, meaning that they occupy a small area in the sky as well as often being situated in front of a large amount of extinction. This minimizes both foreground contamination by field stars and background contamination by giants.

Recent studies of galactic young clusters have been extended down to the hydrogen-burning limit to a distance of 1 kpc (Luhman (1998); Hillenbrand (1997); Carpenter et al. (1997)). These studies suggest that the IMF is universal above 0.1 $M_{\odot}$ (Meyer et al. 2000). The shape of the IMF in the sub-stellar regime is less well constrained and we are only now beginning to probe it in great detail (Hillenbrand & Carpenter (2000); Briceno et al. (2002)). Several clusters have been studied down to 30 M_{Jup} in both photometric and spectroscopic studies, among them the Orion Nebula Cluster (Slesnick et al. (2004)), IC348 (Najita et al. (2000); Luhman et al. (2003a)), the Taurus star forming region (Luhman (2004a); Guieu et al. (2005)), the Chameleon I star forming region (Luhman (2004b)) and the Pleiades (Moraux et al. (2003)).

Searching for IMF variations at the lowest masses can tell us about possible low-mass cut-offs in the IMF, which might be associated with the minimum mass for opacity limited-fragmentation ($\approx$ 10 M_{Jup}) (Rees 1976). Evidence presented by Briceno et al. (2002) (see also: Luhman (2004b)) showed the Taurus star-forming region to exhibit a dearth of brown dwarfs, by as much as a factor of 2, when compared to the denser region of the Orion Nebula Cluster. However, newer studies, covering a larger area of Taurus suggest that this deficiency is not as marked as previously reported (Luhman et al. 2006). Nonetheless the low-mass IMF remains a strong candidate for variations with cluster characteristics. This suggests a possible connection between stellar density and the shape of the low-mass IMF. NGC 1333 is a young star-forming region intermediate in density between Taurus and Orion, making it an ideal test bed to search for variations in the low-mass IMF and explore differences based on star-forming environment.

The NGC 1333 reflection nebula is part of the Perseus molecular cloud complex at an estimated distance of 300 pc (de Zeeuw et al. (1999); Belikov et al. (2002)). The proximity of the cluster allows us to study the IMF down to very low masses. It was first identified as a star-forming region in Herbig & Rao (1972) (see also: Herbig (1974); Strom et al. (1976)). Infrared surveys have since revealed a large population of low-mass objects (Aspin et al. (1994); Lada et al. (1996); Wilking et al. (2004)). These studies have characterized the young stellar population over large areas of the cloud, but have not fully probed the very lowest masses because of a lack of sensitivity.

We have performed a new, deep ($J < 21^m$) near-infrared survey over a limited area in NGC 1333 using NICMOS/HST. This study is complete to fainter magnitudes than previous

studies, thus allowing the characterization of a significant extinction-limited sample of brown dwarfs. This enables us to study the population of very low-mass objects in detail. We obtained photometry as well as infrared spectroscopy. The spectra enable estimates of stellar masses and ages for individual objects by comparing their positions in the H-R Diagram with PMS evolutionary models. The spectra further help us adopt models to interpret our flux-limited survey by constraining a mass-luminosity relation appropriate for the cluster. We construct an extinction limited sample to explore the shape of the mass function in the cluster.

The paper is structured as follows. Section 2 describes the observations and data reduction, followed by a description of the photometric and spectroscopic analysis in Section 3. Section 4 details the results, and places them in context with recent literature. A summary and conclusions are presented in Section 5.

2. Observations and Data Reduction

We obtained images of the young cluster NGC 1333 using camera 3 of NICMOS (NIC3) as part of the HST program 9846. Six fields, each 51.2" x 51.2" with a plate scale of 0.2"pixel^{-1}, were obtained between 2004 Jan 15 and 2005 Aug 11 using 12 HST orbits. In addition to the 6 NGC 1333 fields we also obtained observations for 7 additional objects. Six of these are previously confirmed brown dwarfs from older star-forming regions and the field. We obtained these observations in order to explore the surface gravity dependence of our spectral typing technique. The coordinates for each of the fields in addition to the total exposure times are listed in Table 1. For the position of our fields with respect to molecular line maps of the region please see Figure 1 in Wilking et al. (2004). Each field was observed in F110W, F160W and the grism G141, which cover 0.8 - 1.4 μm (broadband), 1.4 - 1.8 μm (broadband) and 1.1 - 1.9 μm (dispersed), respectively. F110W is roughly equivalent to J-band and F160W is roughly equivalent to H-band. The fields were observed in a 2 x 2 dither pattern, with an offset of 1.75 pixels. The observations were subdivided into visits, with each visit covering one field in G141, F160W and F110W in that order. Since the grism G141 is slitless, stars that are close in either the x or the y direction can have overlapping spectra for each individual visit. To minimize this overlap we observed each photometric and spectroscopic field in 3 visits, at roll angles offset 30 - 75^o and 105 - 150^o between subsequent visits. We were unable to obtain 3 separate roll angles for the fields N2 and N7 causing their final photometry to be less deep than that of the other 4 fields. For this reason they are only used in the spectroscopy section and excluded from the photometric analysis. All 4 of these fields lie in the southern half of the cluster and the complete area

covered by our photometric survey is 2.9 arcmin^2. Compared to the combined areas of the surveys by Wilking et al. (2004) and Aspin et al. (1994), which surveyed both the north and south components of the cluster and covered 79 arcmin^2 and 81 arcmin^2 respectively, our photometric survey thus covers $\approx 2\%$ of the area of NGC 1333. Total integration times for the fields with 3 roll angles, including dithers and multiple roll angles were 383 s for F160W, 766 s for F110W and 4608 s for G141 per field.

2.1. Photometry

Data reduction was carried out using a combination of IRAF and custom IDL routines. The methods described below closely follow those used in W. Liu et al. (2003). The images were dark and sky subtracted using combined dark plus sky frames created with the routine NICSKYDARK in the NICRED package for IRAF (McLeod 1997). Cosmic rays and bad pixels were located and removed using the routine FULLFITBAM, by searching for discontinuities in the flux in each pixel over time. After dark and sky subtraction and cosmic ray reduction, there did not appear to be any bias offsets or "pedestal effects" between the different quadrants of the NICMOS chip, which is a common problem experienced with NICMOS (e.g. W. Liu et al. (2003)). This is because our fields were not very crowded and did not show significant nebulosity, as the pedestal is also dependent on the total charge of the quadrant. The only field that shows any nebulosity is S2. Finally, the images were flatfielded using the routine NICFLATTEN and the appropriate epoch on-orbit flatfields from the Space Telescope Science Center Institute (STScI) website. The dithers were then combined using the IDL software IDP3 (Lytle et al. 1999), aligning the different frames by their World Coordinate System as well as resampling the images by a factor of 2 using a bi-cubic sinc to increase the resolution of the images. The three roll angles were combined using IDP3, first rotating the images to align in angle and then shifting the images to correct for offsets in x and y. For both of these routines, flux was conserved.

All sources presented in the Color-Magnitude Diagram (CMD) (Sec. 3.3) were detected in both the F160W and F110W filters using the IRAF routine DAOFIND with a 10 σ detection threshold. Even with the low amount of nebulosity every image still had some spurious detections which were removed by visual inspection. We took advantage of the three roll angles for each field to help identify false detections. If a source appeared in the same position for each roll angle, it was assumed to be genuine. False detections were located at their position on the chip for only one roll angle.

Since the fields were not crowded, the photometry was performed using the IRAF routine APPHOT. The optimal aperture size was calculated to be 8 pixels in radius with the

sky background measured using an annulus between 10 and 12 pixels around each object. Aperture corrections were calculated out to 25 pixels using several bright, non-saturated stars and applied to the photometry. The aperture corrections derived were 0.054 ± 0.008 mag for m110 and 0.073 ± 0.008 mag for m160, where m110 and m160 refer to the magnitudes associated with F110W and F160W, respectively. Errors in the photometry were computed using PHOT and agreed with errors computed by comparing photometry derived from each separate roll angle. Two objects, ASR 9 and ASR 28, showed close companions. For these an aperture radius of 3 pixels was used with appropriate aperture corrections of 0.32 ± 0.03 mag for m110 and 0.38 ± 0.02 mag for m160 and a sky annulus of 20 to 24 pixels so as to exclude flux from the companion. In addition, one object, ASR 16, appears to have extended nebulosity associated with it. Because of this, photometry was extracted for this object in the same manner as the binaries to minimize contamination from the nebulosity. This source is further discussed in section 4.2. A total of 25 unique sources were detected and are listed in Table 2.

NICMOS magnitudes were calibrated using zero-points of 1775 and 1093 Jy and were calibrated to the Vega system using the conversions of 2.873 x 10^{-6} and 2.776 x 10^{-6} Jy ADU^{-1} s^{-1} for F110W and F160W respectively. Detection limits were assessed using artificial star tests. Artificial stars were added to the images in 0.5 magnitude steps using a PSF derived from bright, non-saturated sources. The recovery fraction of these stars was then computed using the same detection technique as described above. The 90% completeness limits were found to be m160 $\approx 20.5^m$ and m110 $\approx 21.0^m$. The NICMOS magnitudes m110 and m160 were transformed to the CIT system, J and H, by comparing magnitudes for sources in the survey which also had 2MASS photometry (a total of 12 objects). The 2MASS photometry was converted to the CIT system using the transformations of Carpenter (2000). A linear regression was then performed to obtain color transformations between the HST magnitudes and the CIT system. The following color corrections were determined:

$$H = m160 + (0.189 \pm 0.030) + (0.120 \pm 0.025)(m110 - m160)$$
$$J - H = (0.132 \pm 0.073) + (0.760 \pm 0.060)(m110 - m160)$$

These color transformations were used to transform the NICMOS magnitudes to CIT with the J magnitudes calculated as J = (J-H) + H.

Relative astrometry for each object was determined using the World Coordinate System in the header of the NICMOS images together with the XY2SKY routine in the WCSTools package (Mink 2002). The derived astrometry was compared with previously determined coordinates from 2MASS and showed no systematic offset. All coordinates presented in Table 3 are estimated to be accurate to ≤ 1.5".

2.2. Spectroscopy

The spectroscopic observations were performed with the grism G141, which is centered at 1.4 μm, with a wavelength coverage between 1.2 μm - 1.9 μm and a resolution of ≈ 200 per pixel. This covers the water-band feature at 1.4 μm which is expected in the atmospheres of cool objects and is difficult to observe from the ground, making HST ideal for these observations. To reduce these data, the images were first run through the HST pipelines CalnicA and CalnicB. These pipelines perform the dark subtraction, using artificial dark frames from the STScI website, as well as cosmic ray reduction. The pipelines were not used to co-add either the dithers or the roll angles, because this did not improve the quality of the spectra over extracting them from individual images. This means that for each object in the NGC 1333 sample there can be a maximum of 12 extracted spectra. The spectra were extracted using a custom IDL routine NICMOSlook (Pirzkal et al. 1998), which was designed to deal specifically with NICMOS grism data. NICMOSlook reduces spectra in a standard way, by tracing the spectrum across the chip and summing the flux in the spatial dimension as well as subtracting a background region set by the user at each wavelength. To extract spectra, NICMOSlook needs a spectroscopic as well as a photometric image, to perform the wavelength calibration. The photometric image gives the true location of the object's position, which then gives the zero point for the wavelength of the spectrum. The photometric image used was the F160W image because its central wavelength is closer to the central wavelength of G141. The spectra were extracted with an extraction width of roughly 2 x FWHM of the spectra, in general ≈ 4 pixels. The background size was varied depending on the crowding of the field. NICMOSlook also flatfields the spectra during the extraction. This is necessary because the quantum efficiency of the detector changes with both wavelength and position. For this reason the spectra cannot be flatfielded before extraction. NICMOSlook flatfields the spectra using a set of narrowband flatfield images, which are chosen according to the date of the observations, from which the software constructs a 3-dimensional calibration datacube.

Signal-to-noise ratios (SNR) were estimated for all extracted spectra in two ways. First, a 3rd order polynomial was fitted to the combined average spectrum in the spectral region between 1.5 - 1.8 μm and the RMS of the difference between the observed continuum and the fit per pixel calculated. Second, a SNR was calculated for each individual pixel in the spectrum, by estimating the signal as the mean of each pixel and the noise as the error in the mean from the ensemble of individual spectra for each source. Since there are only four independent extractions for some of the spectra, the error in the mean is not necessarily a high fidelity estimate for the noise in each pixel. This means that the SNR estimated in this way may overestimate the real SNR of the spectra. The SNR of the spectrum is then the average of the SNR for all the pixels.

2.3. Spectral Standards

To help calibrate our method for spectral typing we obtained spectra of 7 objects with previously known spectral types (see Table 1), six of which are brown dwarfs. These objects are older than the NGC 1333 sources and were observed to explore the surface gravity dependence in our spectral typing technique. Of the 7 objects, only 4 had high enough SNR to be included in the spectral sequence. They span a spectral range from M8 to L7. In addition we extracted spectra from archival HST grism data (Program IDs #7322 and #7830; see also Najita et al. (2000)) of old low-mass field dwarfs with known spectral types. They span a spectral range from M0 - L5. The spectra are plotted in Figures 1 and 2. All standards used in the spectroscopic analysis are listed in Table 3.

2.4. NGC 1333 Spectra

Spectra were extracted for a total of 14 objects in NGC 1333 from 6 fields. Depending on the position of the spectra on the chip, such as proximity to other objects and position with respect to the edge of the chip, between 4 and 12 spectra were extracted for each source. The spectra were then combined in a sigma-clipped way, excluding pixels which deviated by more than three sigma. For the NGC 1333 objects the SNRs ranged from ≈ 30 to ≈ 100 and the different SNR estimates agreed well with each other. We compared these values with the expected SNR from the STScI exposure time calculator. In general these theoretical SNR tended to be higher than those estimated from the real spectra. We chose to adopt the SNR estimates from the polynomial fits. Spectra of all NGC 1333 objects are plotted in Figure 3.

3. Analysis

3.1. Spectroscopic Analysis

Spectral typing was performed using a water vapor absorption index centered on the water band at 1.4 μm. This band is sensitive to temperature in cool stars later than M0 (Jones et al. 1994) but not strongly dependent on surface gravity (Gorlova et al. (2003); Wilking et al. (2004)). The method described here is similar to the one detailed in Wilking et al. (1999) and Wilking et al. (2004). We define a Q index that is independent of reddening, using the reddening law of Cohen et al. (1981):

$Q = (F1/F2)(F3/F2)^{0.567}$

where F1, F2 and F3 are the averaged fluxes in the bands 1.30 - 1.35 μm, 1.40 - 1.45 μm and 1.65 - 1.70 μm respectively. The index is independent of reddening because it includes only a ratio of flux bands which have been scaled by an exponent directly related to the applicable reddening law. This accounts for any inherent slope in the spectrum due to interstellar reddening and corrects for it. To optimize our spectral typing technique we chose among several different combinations of flux bands and determined which fit of Q versus spectral type for our spectral standards showed the lowest combined error in slope and intercept and at the same time showed the strongest evolution with spectral type. This index was chosen because of its tight fit and its strong evolution with spectral type, as it directly measures the evolution in the depth of the water band feature at 1.4 μm. The evolution of Q with spectral type for the NGC 1333 objects is shown in Figure 3. The uncertainty in Q was estimated by calculating Q for each individual spectrum of an object and then deriving the error in the mean of those values from the multiple spectra which were available for each object. To calibrate the relation between Q and spectral type, a weighted linear fit of Q vs. spectral types for the old field dwarf standards and the young confirmed brown dwarfs was performed. Together these standards have spectral types ranging between M0 - L7 (see Table 3). Spectra with types earlier than M0 were excluded because they show no water band absorption. This fit gives the relation:

$$MV(subclass) = (-5.04 \pm 0.31)Q + (-2.22 \pm 0.47)$$

The fit, together with the Q values for the field dwarfs, is plotted in Fig. 4.

We tried to assess the surface gravity dependence of the Q index by deriving a fit of Q vs. spectral type for the young brown dwarfs with known spectral types observed as part of our program. Field stars in general have log(g) = 5.0 - 5.5, while younger PMS stars have lower surface gravities between log(g) = 3.0 - 4.2 (Gorlova et al. 2003). Thus it is important to explore whether our spectral typing technique is valid across a range of log(g). We performed a fit using only the young confirmed brown dwarfs and compared it to the fit derived using the field dwarf standards. Comparing these two fits, we estimate that assigning spectral types using the old M dwarfs might underestimate their temperature by $\approx$ 200 K (too late by one subclass). This means the temperatures we derive are lower limits, similar to previous findings by Gorlova et al. (2003) and Wilking et al. (2004). We only have high SNR spectra for 3 young brown dwarfs however, and so these are preliminary results at best.

Table 4 shows the derived spectral types for the NGC 1333 objects. The spectral types derived for the NGC 1333 objects range from <M0 to M8. Stars with no water band absorption features were assigned a spectral type of <M0. Uncertainties in Q were between $\pm$0.01 - 0.17, which leads to uncertainties in spectral types of approximately one subclass,

comparable to the potential error in our calibration mentioned above. From this relation we classify seven objects with spectral types of M6-M8 which are likely brown dwarfs. Three of the objects for which we have derived spectra, ASR 24, ASR 15 and ASR 17, have previous spectral classifications using K-band H_2O absorption bands (Wilking et al. 2004). Both derived spectral types are listed in Table 4 and agree to within the errors. While we did not detect cooler young brown dwarfs than Wilking et al. (2004), we were able to observe similar objects with greater obscuration. Alternative methods of the spectroscopic reduction as well as a method of spectral typing are also addressed in detail in Fanetti (2005).

3.2. H-R Diagram

To estimate the age of the cluster we compared the positions of the NGC 1333 PMS objects in the H-R Diagram to theoretical evolutionary tracks by D'Antona & Mazzitelli (1997;1998) (hereafter DM98) as appropriate for the median cluster age characterizing the low mass population. First, we converted spectral types derived for the NGC 1333 objects to temperatures using empirical relations derived from Dahn et al. (2002) and Leggett et al. (1996). The typical uncertainties in temperatures due to uncertainties in spectral types were $\approx$ 200K. Luminosities were derived from the de-reddened J-band magnitudes. To determine M_J we first calculated visual extinctions using the standard relation A_v=9.09x[(J-H)$_{obs}$ - (J-H)$_o$] (Cohen et al. 1981) where (J-H)$_o$ is the intrinsic color for a given spectral type. The values of A_v derived for NGC 1333 sources lie between 0 and 14 mag, with 6 sources having an extinction higher than 5 mag. Values for $\log(L_{bol}/L_\odot)$ were calculated from the de-reddened J-band magnitudes, after bolometric correction, as $\log(L_{bol}/L_\odot) = 1.89 - 0.4\ M_{bol}$. We adopt intrinsic colors and bolometric corrections following Wilking et al. (2004). Typical errors in $\log(L_{bol}/L_\odot)$ are $\pm$ 0.2 dex and are derived based on errors in the J-band magnitude, the distance modulus and the bolometric correction. The H-R Diagram is presented in Figure 5. The luminosities and temperatures for the NGC 1333 objects with spectral types are listed in Table 4. The positions of the brown dwarfs are compared to the theoretical tracks and isochrones from the models of DM98. In addition to our sample, objects in NGC 1333 for which unique spectral types were derived in Wilking et al. (2004) are plotted on the H-R diagram. From these objects we estimated the cluster to be younger than 1 Myr and chose the DM98 0.3 Myr tracks as appropriate for the median cluster age. It is noteworthy that these ages are relative ages as absolute ages are model dependent. The objects in the HR Diagram show a scatter around the median age with an overall trend to younger ages for lower mass objects. The scatter is due in part to errors in the luminosities of the objects introduced by errors in the photometry and dereddening. The overall trend towards younger ages for lower mass objects is an effect often observed in HR Diagrams of young stellar clusters. This is

most likely an effect of imperfect PMS models and not a real effect of an age-mass relation for the cluster. The median age of 0.3 Myr for our H-R diagram corresponds to the break point of the mass bins for our analysis (0.1 $M_{\odot}$), thus ensuring that we are using the correct mass-luminosity relationship at that mass.

Four objects exhibit unusual positions in the H-R Diagram, with ages much older than 1 Myr, appearing under-luminous compared to their PMS counterparts. Two of these objects have spectral types earlier than M0, meaning they show no water band absorption feature in their spectra. These two objects could be background stars. The other two objects, both of spectral type M4 also appear fainter than expected, but could still be cluster members. Notice also 3 objects from Wilking et al. (2004) which lie below the expected locus for the majority of the PMS objects. These objects are specifically addressed in Wilking et al. (2004), but the following reasoning applies to them as well. The sources could have an infrared excess, causing a dilution of the water absorption bands, leading us to assign a spectral type that is too early. They could also exhibit unresolved scattered light due to a surrounding disk, which would result in bluer colors and could cause us to underestimate extinction and thus luminosity. There is evidence that disks around young brown dwarfs are ubiquitous. M. Liu et al. (2003) for example found that 77% of a sample of young brown dwarfs in IC348 and Taurus showed evidence of a circumstellar disk. To establish whether any of these objects show signs of a disk and thus confirming their youth, we attempt to assess whether they show an infrared excess in the next section. This method is described in detail in Wilking et al. (1999). Since we cannot rule out either solution at this point it is impossible to assign a mass to the two M4 sources or an age if they are not cluster members. For these reasons all four sources have been excluded from the mass function analysis. It is possible that other objects in our sample also possess circumstellar disks. However, for most objects we can expect the effect of the disks on spectral typing to be small (Meyer et al. (1997); Muzerolle et al. (2003)). Even if objects show a strong infrared excess only those with special viewing geometry would be dominated by scattered light leading us to underestimate the reddening. Further observations will be required to test whether these objects suffer from the effects mentioned.

3.3. K-band excess

For NGC 1333 objects with 2MASS photometry we have estimated the amount of excess emission at K, defined as r_k=F_{Kex}/F_K[1], where F_{Kex} is the flux contribution at K

[1] $r_k = F_{Kex}/F_K = [(1+r_\lambda)(10^{[(H-K)-(H-K)_o-0.065A_v]/2.5})$-1]. We have assumed that r_j=r_h=0.

due to circumstellar material and F_K the inherent stellar flux at K (Wilking et al. (2004); Wilking et al. (1999)). Values of r_k are listed in Table 4. These estimates are lower limits since we have assumed no excess at J- or H-band. Two objects, ASR25 and ASR105, show moderate K-band excesses. ASR25 has a peculiar position on the H-R Diagram as mentioned above. The measured K-band excess makes it a likely cluster member and it may indicate that we have assigned it a spectral type that is too early, which would make it a brown dwarf, and that it may possess a disk. Most of the other objects show little or no excess emission. It is possible that the lowest mass objects possess disks which are too cool to cause an excess in the K-band as inner disk temperature is expected to be correlated with stellar luminosity (Pascucci et al. (2003)).

3.4. Color-Magnitude Diagram and Extinction-Limited Sample

In Figure 6 we present a CMD for the cluster. Also shown is the 0.3 Myr isochrone of DM98, which we adopted based on the H-R diagram discussed above. The isochrone was converted to the CMD by using a set of colors and bolometric corrections, with colors taken from Leggett (1992), while bolometric corrections were adopted from Leggett et al. (1996), similar to Wilking et al. (1999). All but 3 out of 25 objects in the CMD appear to lie below the hydrogen burning limit for a cluster age of 0.3 Myr. This number changes to 5 if we instead assume a cluster age of 1 Myr. The photometry, isochrone and reddening vector (Cohen et al. 1981) are all presented in the CIT system and the completeness limit discussed above is also shown. For the age derived above we define an unbiased sample of low-mass objects in order to constrain the IMF for the cluster. We begin by creating an extinction-limited subsample, to ensure that we are sampling the stellar population uniformly and not over-representing more luminous (massive) deeply embedded objects. The extinction limits used are $A_v \leq 21.1$ mag and ≤ 18.3 mag for the 0.3 Myr and 1 Myr DM98 isochrones respectively, corresponding to a mass range of 0.02 $M_\odot$ - 0.1 $M_\odot$. For both isochrones this led to a total sample of 13 (17-4) objects, excluding the 4 objects mentioned in section 3.2.

We are sensitive to a mass range lower than 20 M_{Jup}, albeit for a smaller range of extinctions. However, the DM98 tracks do not extend below this mass limit. Thus no objects lower than 20 M_{Jup} were considered for the cluster mass function. This means that compared to the survey of Wilking et al. (2004) we probe to a higher A_v but not to a lower mass range. There are six objects lying in the region below 20 M_{Jup} for an assumed age of 0.3 Myr, two of them very close to the 90% completeness limit. One of them, ASR 28b, is a suspected companion to a brown dwarf primary and will be dealt with in more detail in Section 4.3. Another object has been previously classified as ASR 16 and appears to have

extended nebulosity associated with it. There are tracks available that extend below 20 M_{Jup}, such as Baraffe et al. (1998) and Burrows et al. (1997). However the NGC 1333 objects lie above the youngest tracks available for both sets of models (1 Myr) in the H-R Diagram. Thus these tracks are most likely not appropriate for NGC 1333, making the DM98 tracks the most appropriate choice for NGC 1333, with a median age of 0.3 Myr. Typical errors in assigning masses from different tracks are approximately a factor of 2 (White & Hillenbrand 2004) although this is only well tested down to ≈ 0.3 $M_{\odot}$.

It is also worth noting that while the rapid drop in the number of objects below 20 M_{Jup} looks striking, a fairly large area in the CMD in that region is covered by a small range in mass namely between 5 - 20 M_{Jup}, with the masses defined according to tracks by Baraffe et al. (1998) and Burrows et al. (1997). It is however curious that the objects we do detect seem clustered towards the lower end of this mass range, which is close to our 90% completion limit. We detect no objects between 10 - 20 M_{Jup} with low A_v. Due to our small sample size and survey area this does not allow us to rule out that such objects exist in the cloud. It is however suggestive that NGC 1333 may lack objects below 20 M_{Jup}.

It is possible that at least some of the objects are background contaminants. We have tried to assess the amount of background contamination by adjusting the number counts measured by Lucas et al. (2003) in the Hubble Deep Field South (HDF-S) using F160W. Using their estimates for number counts one expects 1.7 +0.4/-1.1 objects between 19^m - 21^m in our survey. However, the HDF-S points out of the Galaxy and thus this number should be a lower limit since NGC 1333 lies closer to the Galactic plane. On the other hand our NGC 1333 fields lie in front of a large amount of extinction, which will reduce the number of contaminants.

4. Discussion

4.1. Cluster IMF

To constrain the slope of the IMF down to the lowest masses in the cluster we derive the ratio of very low-mass stars (0.076 - 0.1 $M_{\odot}$) to brown dwarfs (0.02 - 0.076 $M_{\odot}$) in our survey. We calculate this ratio to be $R = 3/10 = 0.30 \pm 0.20$ assuming a 0.3 Myr isochrone, with the errors computed due to Poisson statistics. For a 1 Myr isochrone this ratio increases to R = $5/8 = 0.625 \pm 0.356$. Both cluster ages give ratios consistent with having been drawn from a Chabrier (2003) system IMF, which gives a most likely ratio (mode) of R = 0.30. This corresponds to a slope of $dN/dM \propto M^{-1.1}$ over this range. For the older isochrone there are a larger number of low-mass stars but still more brown dwarfs due to the hydrogen burning

limit shifting to a fainter magnitude for a higher cluster age. Both ratios are lower limits, since the low-mass bin has objects for which we do not have spectra and thus contamination by field stars may lead us to overestimate the number of brown dwarfs relative to low mass stars in the sample. Above 0.076 $M_\odot$ all objects but one have assigned spectral types which allow us to assess their cluster membership. The object without a spectral type is ASR9a which is a previously identified cluster member (Aspin et al. 1994) which we have resolved to be a binary. Below 0.076 $M_\odot$ however, apart from ASR 9b, there are four objects without spectral types, which could be possible field stars. Thus these ratios imply upper limits for the slope of the cluster mass spectrum below 0.1 $M_\odot$ of $\alpha \leq 1.1$ and $\alpha \leq 0.55$ for 0.3 Myr and 1 Myr isochrones respectively, where $dN/dM \propto M^{-\alpha}$ and $\alpha = 2.35$ is the Salpeter slope.

Where does our result stand with regard to comparable clusters and studies? Wilking et al. (2004) have explored the mass spectrum of NGC 1333 using an extinction limited sample down to 0.04 $M_\odot$ finding the ratio of sub-stellar (0.04 - 0.1 $M_\odot$) to stellar objects (0.1 - 1 $M_\odot$) to be $R_{SS} = 1.11$ +0.8/-0.4. They used this to estimate an upper limit for the slope of the lower end of the mass function of $\alpha \leq 1.6$. This compares well with slopes in the solar neighborhood below the hydrogen-burning limit, which Reid et al. (1999) found to be $1 < \alpha < 2$. Allen et al. (2005) have further attempted to constrain the shape of the field star IMF below 0.1 $M_\odot$ and found $-0.6 < \alpha < 0.6$ with 60% confidence and a best fit of $\alpha = 0.3$.

To derive a broader estimate of the cluster mass function we attempted to combine this survey with that of Wilking et al. (2004) to make the cluster mass function more easily comparable to ratios published for other regions. We combined all objects between 0.1 - 1 $M_\odot$ from Wilking et al. (2004) with an extinction limit of $A_v \leq 12.8^m$ with the HST objects between 0.03 - 0.1 $M_\odot$ with an extinction limit of $A_v \leq 21.1^m$, scaling the number of HST objects by the ratios of the survey areas, which is 26.3, as well as the extinctions, which is 0.61. We chose not to include the objects below 0.1 $M_\odot$ from Wilking et al. (2004) as that survey was estimated to have a large field star contamination below 0.1 $M_\odot$. We compute this ratio as $R_1 = N(0.1 - 1\ M_\odot)/N(0.03 - 0.1\ M_\odot) = 0.14 \pm 0.047$ with errors again due to Poisson statistics, using the same cluster age and models for both surveys. This ratio is abnormally low when compared to other published results in this mass range even within the errors. We have recomputed this ratio for 5 different young star clusters based on previously published data sets and results range between $\approx$ 3 - 6. All surveys were either extinction limited surveys or were normalized to make them as close to extinction limited surveys as possible. See Table 5 for computed results and errors.

We then tried to compensate for possible differences in stellar density between the two surveys by introducing a normalization factor in an overlapping mass range between 0.07 - 0.1 $M_\odot$. This normalization factor was computed to be 3.5 ± 2.0. This increases the ratio to

$R_2 = 0.64 \pm 0.38$, which is higher but still significantly lower than the result for any other cluster. This survey was centered on known brown dwarf candidates. Could this bias our result towards an artificially high number of brown dwarfs? Each of our fields was centered on one brown dwarf candidate, with S3A and S3B including the same candidate but offset from each other. If we remove these three candidates from our ratio, the normalized ratio increases to $R_3 = 0.83 \pm 0.41$, which is consistent with the ratio previously determined. Thus the inclusion of these objects does not fundamentally change our results.

Due to the expected field star contamination in Wilking et al. (2004) both ratios are lower limits. However, if the observed density of brown dwarfs is constant over the molecular core previously surveyed at near-infrared wavelengths, this would imply that brown dwarfs outnumber low-mass stars in the cloud. This may be some indication that brown dwarfs form in a clustered environment within the cloud or are spatially segregated from stars due to dynamical evolution.

4.2. Pre-Main Sequence Activity

Getman et al. (2002) have conducted a Chandra X-Ray study of young stellar objects in NGC 1333. Two objects in our study, ASR8 and ASR24, show signs of x-ray activity. Both are spectroscopically confirmed brown dwarfs and have virtually no extinction. This means that 2 of our 8 (excluding the 4 sources discussion in Sec. 3.2) or 25% of our spectroscopically confirmed brown dwarfs are detected in the X-Ray. However, most of the other spectroscopic brown dwarfs in our survey have higher extinctions, decreasing the chance of detecting existing x-ray activity (Preibisch et al. 2005).

One of the objects in our survey, ASR 16, appears to have extended nebulosity associated with it, which is detected only in the F160W image. We were not able to obtain a spectrum for the object or the associated nebulosity. Extended emission in the infra-red can be associated with emission-line Herbig-Haro objects or scattered light envelopes. Since the nebulosity is seen only in the H-band and not at J, contrary to expectations from scattered light models (Gomez et al. 1997) we explore the possibility of an Herbig-Haro outflow associated with this brown dwarf candidate in NGC 1333. Since the nebulosity emission is bright in the F160W filter which covers 1.4 - 1.8 μm it seems that the emission is likely due to [Fe II] at 1.644 μm. Such outflows are thought to be associated with accretion onto the central object. Muzerolle et al. (2005) find signs of accretion are common in the spectra of brown dwarfs. Outflows have also recently been detected around brown dwarfs (Whelan et al. 2005). We tentatively identify this as a candidate outflow around the brown dwarf ASR 16.

4.3. Binaries

There are two sources in our fields which have possible close companions. One was previously identified as ASR 9, which is now resolved into ASR9a and ASR9b, with a separation of 0.8". The other is ASR28a, which we have determined has a close companion ASR 28b. ASR28a is one of our brown dwarf candidates with a spectral type of M7. ASR28a and ASR28b have a separation of 1.2" ($\approx$ 350 AU at the distance of NGC 1333) and ASR28b is 4.2 magnitudes fainter in H. If ASR28b is indeed a cluster member its colors and apparent J-band magnitude (assuming the same A_v as ASR 28a) suggest a temperature of $\approx$ 1800 K (spectral type L4 (Dahn et al. 2002)) and a corresponding mass of 5 M_{Jup} (Burrows et al. 1997) (with an approximate mass ratio of 0.15). If confirmed this object would be very similar to the reported planetary mass companion of 2MASS1207-3923 (hereafter 2MASS1207). ASR28b is too faint to extract a spectrum from this survey and J- and H-band photometry are not enough to rule out the possibility that it is a background object earlier than M4. To ascertain that it is indeed a cluster member we hope to obtain a J- and H-band spectrum of ASR28b in the near future.

5. Summary and Conclusions

We present NICMOS photometry and spectroscopy for 6 regions in NGC 1333 centered on previously detected brown dwarfs from Wilking et al. (2004). We also analyze spectra of brown dwarf standards from this program and that of Najita et al. (2000). Our results are as follows:

- We detect a total of 27 sources at H and 25 sources at J down to $M_J \leq 21^m$ and $M_H \leq 20.5^m$ over a region of 4 x 51.2" x 51.2" square arcseconds.
- Following Wilking et al. (2004) and Wilking et al. (1999) we develop a reddening-independent water band index to estimate spectral types within one subclass from SNR $\geq$ 30 NICMOS G141 spectra. With this method we derive spectral types for 14 sources in NGC 1333 from $\leq$M0 - M8. Seven objects have spectral types $\geq$ M6 suggesting they are young brown dwarfs. While we were sensitive to lower mass objects than Wilking et al. (2004), we detected only objects of comparable mass but with much higher extinction.
- Using the CMD and an assumed age of 0.3 Myr for the cluster we define an extinction limited sample of 13 sources between 0.02 - 0.1 $M_\odot$ with $A_v \leq 21.1^m$. Although we are sensitive to lower A_v objects between 10 - 20 M_{Jup}, none were detected. Though

we are limited by the small number of objects in our survey, this may be indicative of a lack of objects below 20 M_{Jup} in the cloud.

- We compute the ratio of low-mass stars to brown dwarfs in the cluster as R = N(0.076 - 0.1 $M_\odot$)/(0.02 - 0.076 $M_\odot$) = 0.30 ± 0.20, which is consistent with having been drawn from a field-star IMF (Chabrier 2003). We also compute the ratio of stars to low-mass objects in the cluster in conjunction with the survey by Wilking et al. (2004) as R= N(0.1 - 1$M_\odot$)/(0.03 - 0.1$M_\odot$) = 0.64 ± 0.38, which lies below published results for other regions. This may indicate that brown dwarfs form in a segregated environment compared to stars in this cluster.

- Our survey includes several unusual objects, including a possible companion to a spectroscopically confirmed brown dwarf ASR 28, which if it is a cluster member would have a mass of 5 M_{Jup}. In addition one of the brown dwarfs (ASR 16) might have an outflow associated with it, which could be confirmed through follow-up spectroscopy.

This work was supported by a Cottrell Scholar's Award to MRM from the Research Corporation and NASA grant HST13-9846. We would like to thank Morten Andersen for sharing data in advance of publication as well as helpful suggestions. We thank Wilson Liu and Wolfram Freudling for assistance with data reduction and Angela Benoist for preliminary work on spectral reduction.

REFERENCES

Allen, P. R., Koerner, D. W., Reid, I. N., & Trilling, D. E. 2005, ApJ, 625, 385

Andersen, M., Meyer, M. R., Oppenheimer, B., Dougados, C., & Carpenter, J. 2006, AJ, in press

Aspin, C., Sandell, G., & Russell, A. P. G. 1994, A&A, 106, 165

Baraffe, I., Chabrier, G., Allard, F., & Hauschuldt, P.H. 1998, A&A, 337, 403

Belikov, A., Kharchenko, N., Piskunov, A., Schilbach, E., & Scholz, R.-D. 2002, A&A, 337, 403

Briceno, C., Luhman, K., Hartmann, L., Stauffer, J. R., & Kirkpatrick, J. D. 2002, ApJ, 580, 317

Burrows, A., Marley, M., Hubbard, W., Lunine, J., Guillot, T., Saumon, D., Freedman, R., Sudarsky, D., & Sharp, C. 1997, ApJ, 491, 856

Carpenter, J. M. 2000, AJ, 121, 2851

Carpenter, J., Meyer, M. R., Dougados, C., Strom, S. E., & Hillenbrand, L. 1997, AJ, 114, 198

Chabrier, G. 2003, PASP, 115, 763

Chauvin, G., Lagrange, A.-M., Dumas, C., Zuckerman, B., Mouillet, D., Song, I., Beuzit, J.-L., & Lowrance, P. 2005, A&A, 438, 25

Cohen, J. G., Frogel, J. A., Persson, S. E., & Elias, J. H. 1981, ApJ, 249, 481

D'Antona, F., Mazzitelli, I. 1997, in Cool Stars and Associations, eds. R. Pallavicini, G. Micela, Mem. S. A. It., 68, n.4.

D'Antona, F., Mazzitelli, I. 1998, priv. comm.

Dahn, C. C. et al. 2002, AJ, 124, 1170

de Zeeuw, P. T., Hoogerwerf, R., & de Bruijne, J. H. J. 1999, AJ, 117, 354

Fanetti, T. 2005, M.S. thesis, Univ. Missouri St. Louis

Getman, K. V., Feigelson, E. D., Townsley, L., Bally, J., Lada, C. J., & Reipurth, B. 2002, ApJ, 575, 354

Gizis, J. 2002, ApJ, 575, 484

Gizis, J., & Bharat, R. 2004, ApJ, 608, 113

Gomez, M., Whitney, B. A., Kenyon, S. J. 1997, AJ, 114, 1138

Gorlova, N., Meyer, M. R., Rieke, G. H., & Liebert, J. 2003, ApJ, 593, 1074

Guieu, S., Dougados, C., Monin, J.-L., Magnier, E., & Martìn, E. L. 2006, A & A, 446, 485

Henry, T. J., Kirkpatrick, J. D., & Simons, D. A. 1994, AJ, 108, 1437

Herbig, G. H. 1974, Lick Obs. Bull. No. 658

Herbig, G. H., & Rao, N. 1972, ApJ, 174, 401

Hillenbrand, L. 1997, AJ, 113, 1733

Hillenbrand. L. A., & Carpenter, J. 2000, ApJ, 113, 1733

Jones, H. R. A., Longmore, A. J., Jameson, R. F., & Mountain, C. M. 1994, MNRAS, 267, 413

Kirkpatrick, J. D., Henry, T. J., & McCarthy, D. W. 1991, ApJS, 77, 417

Kirkpatrick, J. D., Reid, I. N., Liebert, J., Cutri, R. M., Nelson, B., Beichman, C. A., Dahn, D. C., Monet, D. G., Gizis, J. E., & Skrutskie, M. F. 1999, ApJ, 519, 802

Kroupa, P., Tout, C.A., & Gilmore, G. 1993, MNRAS, 262, 545

Lada, C., Alves, J., & Lada, E. 1996, AJ, 111, 1964

Leggett, S. K. 1992, ApJS, 82 ,351

Leggett, S. K., Allard, F., Berriman, G., Dahn, C. C., & Hauschildt, P. H. 1996, ApJS, 104, 117

Liu, M. C., Najita, J., & Tokunaga, A. T. 2003, ApJ, 585, 372

Liu, W. M., Meyer, M. R., Cotera, A. S., & Young, E. T. 2003, AJ, 126, 1665

Lucas, R. A. et al. 2003, AJ, 125, 398

Luhman, K. 2004, ApJ, 602, 816

Luhman, K. 2004, ApJ, 617, 1216

Luhman, K., Briceno, C., Stauffer, J. R., Hartmann, L., Barrado y Navascues, B., & Caldwell, N. 2003, ApJ, 590, 348

Luhman, K., Joergens, V., Lada, C., Muzerolle, J., Pascucci, I., & White, R. 2006, Protostars and Planets V, in press

Luhman, K., Rieke, G., & Lada, C. 1998, ApJ, 508, 347

Luhman, K., Rieke, G., Young, E., Cotera, A., Chen, H., Rieke, M., Schneider, G., & Thompson, R. 2000, ApJ, 540, 1016

Luhman, K., Stauffer, J. R., Muench, A. A., Rieke, G. R., Lada, E., Bouvier, J., & Lada, C. 2003, ApJ, 593, 1093

Lytle, D., Stobie, E., Ferro, A., & Barg, I. 1999, ASPC, 172, 445

Martin, E. L., Brandner, W., Bouvier, J., Luhman, K. L., Stauffer, J., Basri, G., Zapatero Osorio, M. R., & Barrado y Navascues, D. 2000, ApJ, 543, 299

McLeod, B. A. 1997, in The 1997 HST Calibration Workshop with a New Generation of Instruments, ed. S. Casarteno, R. Jedrzejewski, C. D. Keyes, & M. Stevens (Baltimore:STScI), 281

Meyer, M. R., Adams, F. C., Hillenbrand, L. A., Carpenter, J. M., & Larson, R. B. 2000, Protostars and Planets IV, ed.V.Mannings, A.P. 121

Meyer, M. R., Calvet, N., & Hillenbrand, L. 1997, AJ, 114, 288

Miller, G. E., & Scalo, J. M. 1979, ApJS, 41, 513

Mink, D.J. 2002 in ASP Conf. Ser. 281, Astronomical Data Analysis Software and Systems XI, ed. D. A. Bohlender, D. Durand & T. H. Handley (San Francisco: ASP), 169

Mohanty, S., Jayawardhana, R., & Barrado y Navascues, D. 2003, A & A, 593 109

Moraux, E., Bouvier, J., Stauffer, J. R., & Cuillandre, J.-C. 2003, A&A, 400, 891

Muench, A., Lada, E., Lada, C., & Alves, J. 2002, ApJ, 573, 366

Muzerolle, J., Calvet, N., Hartmann, L., & D'Alessio, P. 2003, ApJ, 597, 149

Muzerolle, J., Luhman, K. L., Briceno, C., Hartman, L., Calvet, N. 2005, ApJ, 625, 906

Najita, J. R., Tiede, G. P., & Carr, J. S. 2000, ApJ, 541, 977

Pascucci, I., Apai, D., & Dullemond, C. P. 2003, ApJ, 590, 111

Pirzkal, N., Freudling, W., Thomas, P., & Dolensky, M. 1998, APSC, 145, 188

Preibisch, T., McCaughrean, M., Grosso, N., Feigelson, E., Flaccomio, E., Gletman, K., Hillenbrand, L., Meeus, G., Micela, G., Sciortino, S., & Stelzer, B. 2005, ApJS, 160, 582

Rees, M. 1976, MNRAS, 176, 483

Reid, I. N., Kirkpartick, J., Burrows, A., Gizis, J. E., Burgasser, A., Dahn, C. C., Monet, D., Cutri, R., Beichman, C. A., & Skrutskie, M. 1999, ApJ, 521, 613

Slesnick, C. L., Hillenbrand, L. A., & Carpenter, J. M. 2004, ApJ, 610, 1045

Sterzik, M., Pascucci, I., Apai, D., van der Blieck, N., & Dullenmond, C. 2004, A & A, 427, 245

Strom, S., Vrba, F., & Strom, K. 1976, AJ, 81, 314

Whelan, E. T., Ray, T. P., Bacciotti, F., Natta, A., Testi, L., Randich, S. 2005, Nature, 435, 652

White, R., & Hillenbrand, L. 2004, ApJ, 604, 741

Wilking, B., Greene, T. P., & Meyer, M. R. 1999, AJ, 117, 469

Wilking, B., Meyer, M. R., Greene, T. P., Mikhail, A., & Carlson, G. 2004, AJ, 127, 1131

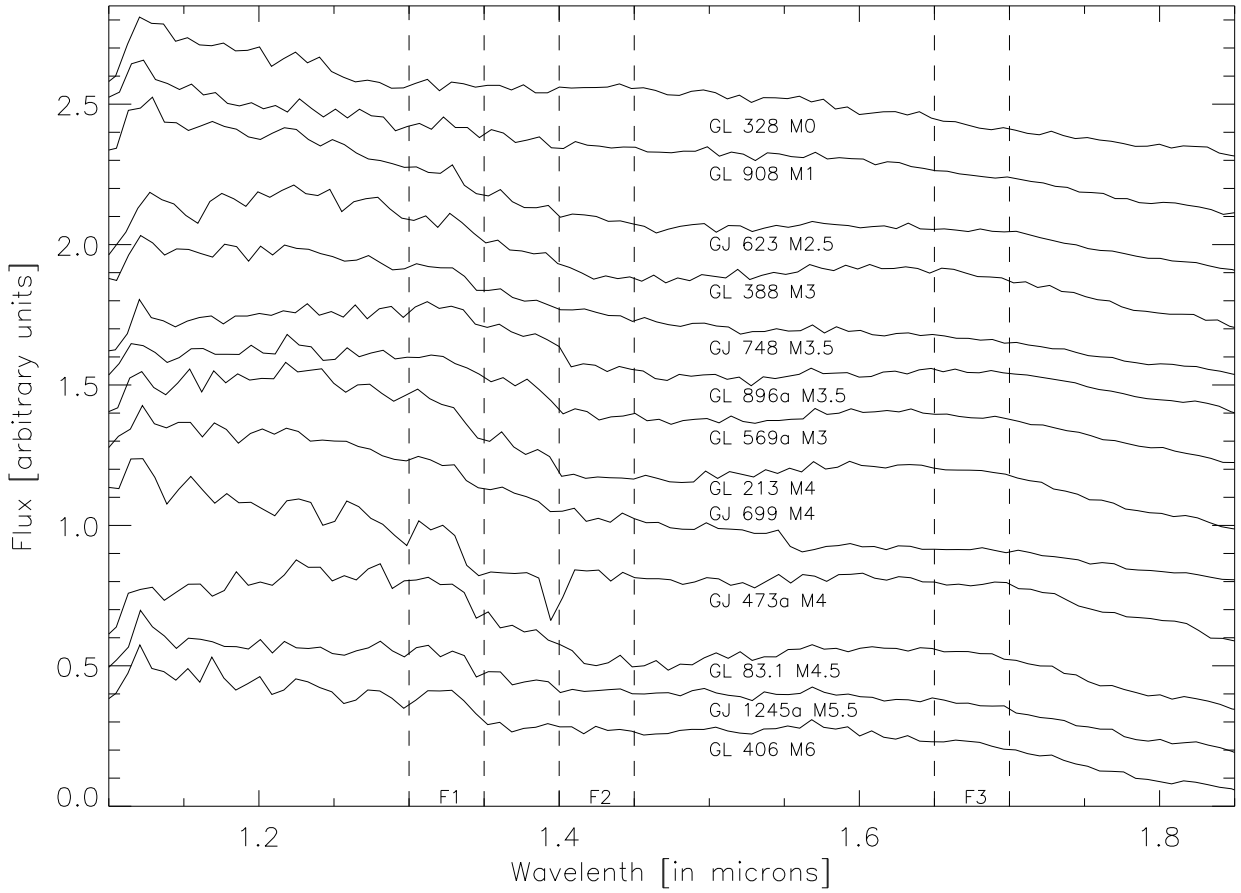

Fig. 1.— NICMOS G141 spectra of field dwarf standards from M0 - M6.

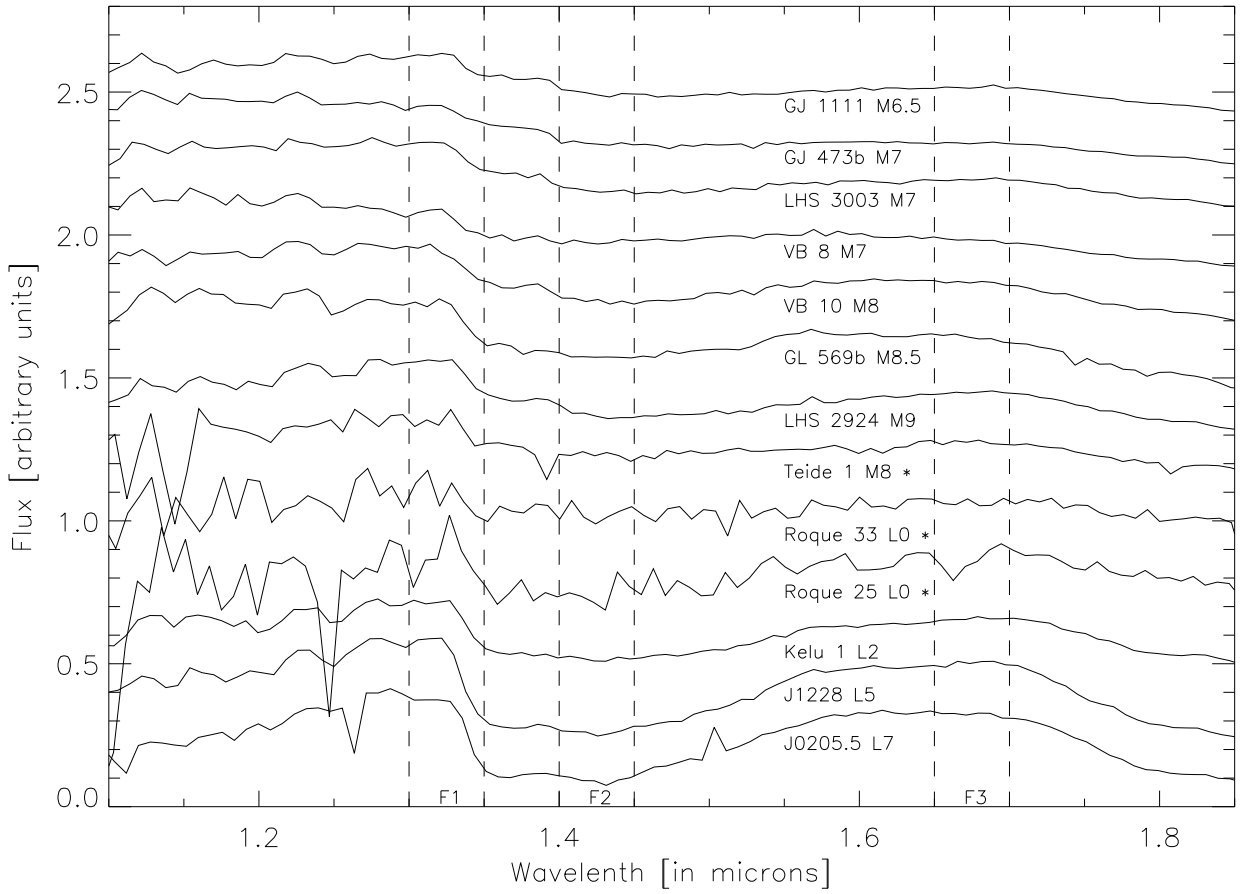

Fig. 2.— NICMOS G141 spectra of field dwarf standards as well as younger brown dwarfs confirmed through visible spectroscopy between M6.5 - L7. The younger brown dwarfs are denoted by an asterisk.

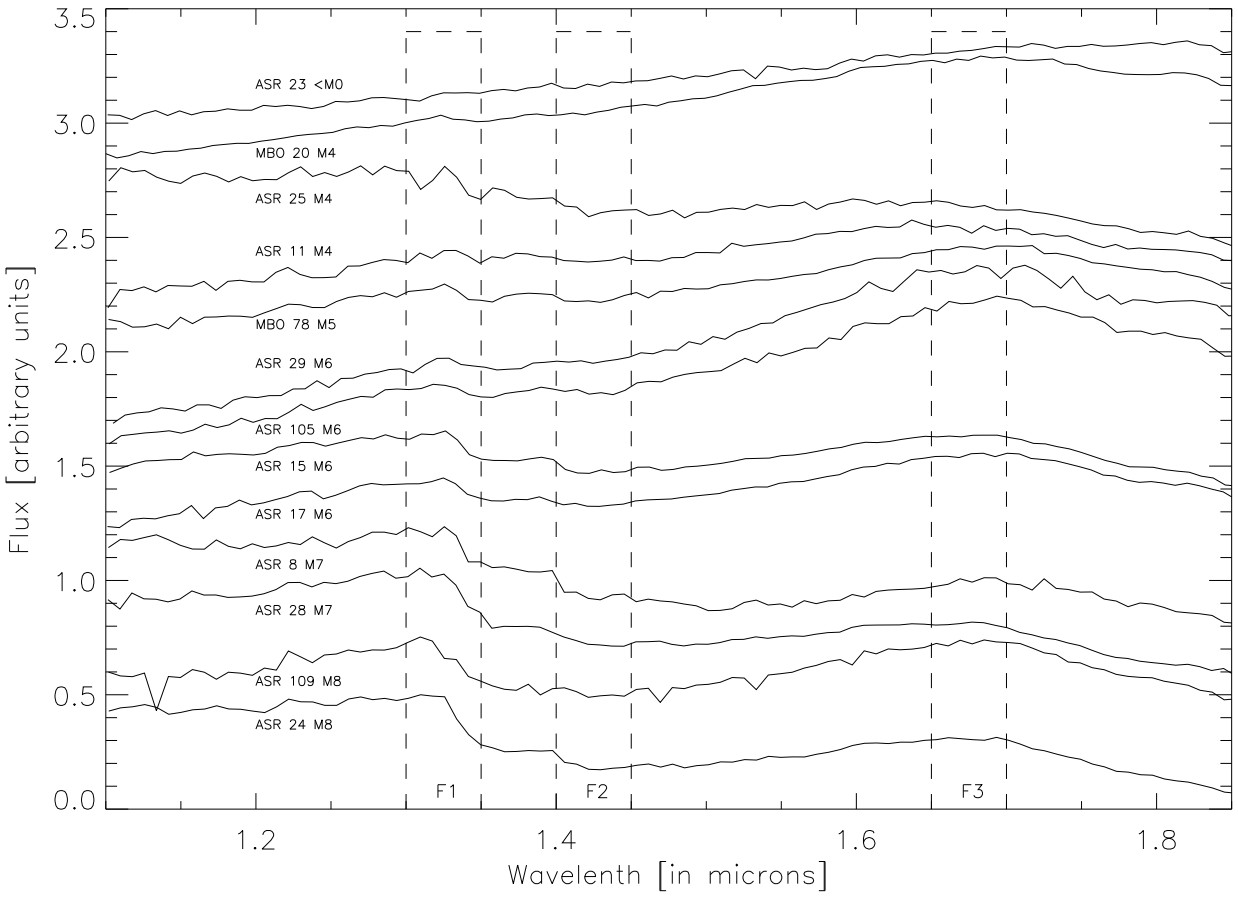

Fig. 3.— NICMOS G141 spectra for candidate brown dwarfs located in NGC 1333, arranged from earliest to latest spectral type.

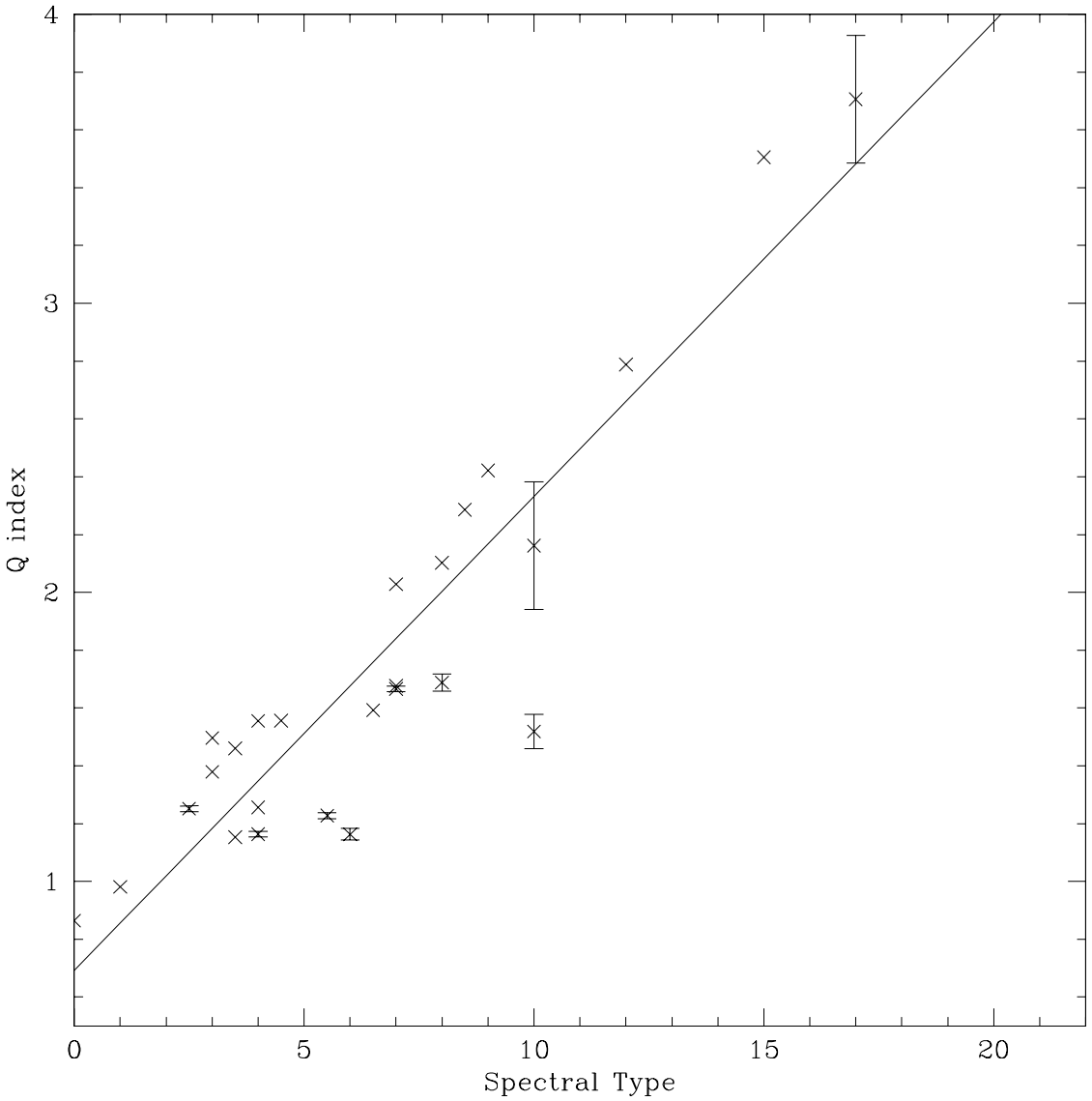

Fig. 4.— Plot of Q vs. spectral type showing the fit derived for the old field dwarfs and young brown dwarfs.

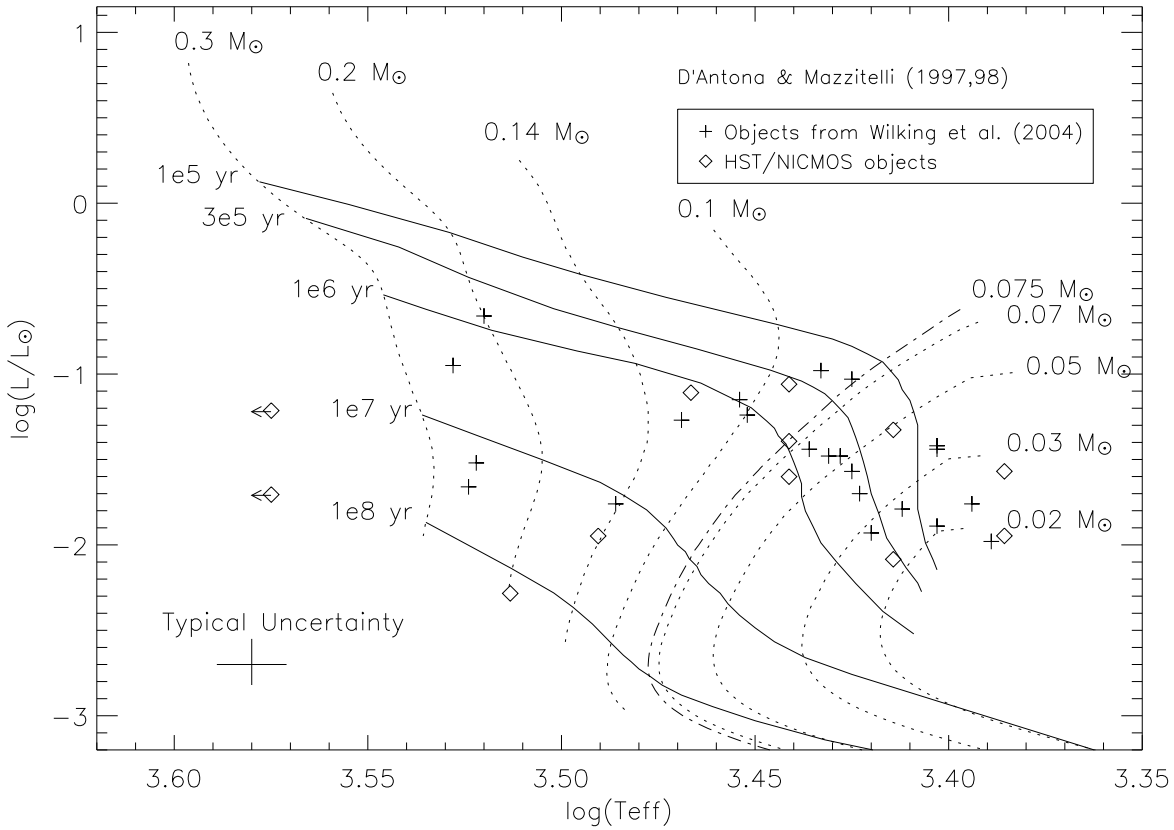

Fig. 5.— H-R Diagram of the NGC 1333 objects from our survey overplotted on DM98 isochrones and tracks as well as sources from Wilking et al. (2004). For sources in common between the two studies we defer to this study. Four objects show unusual positions in the H-R Diagram. They are commented upon in detail in section 3.2.

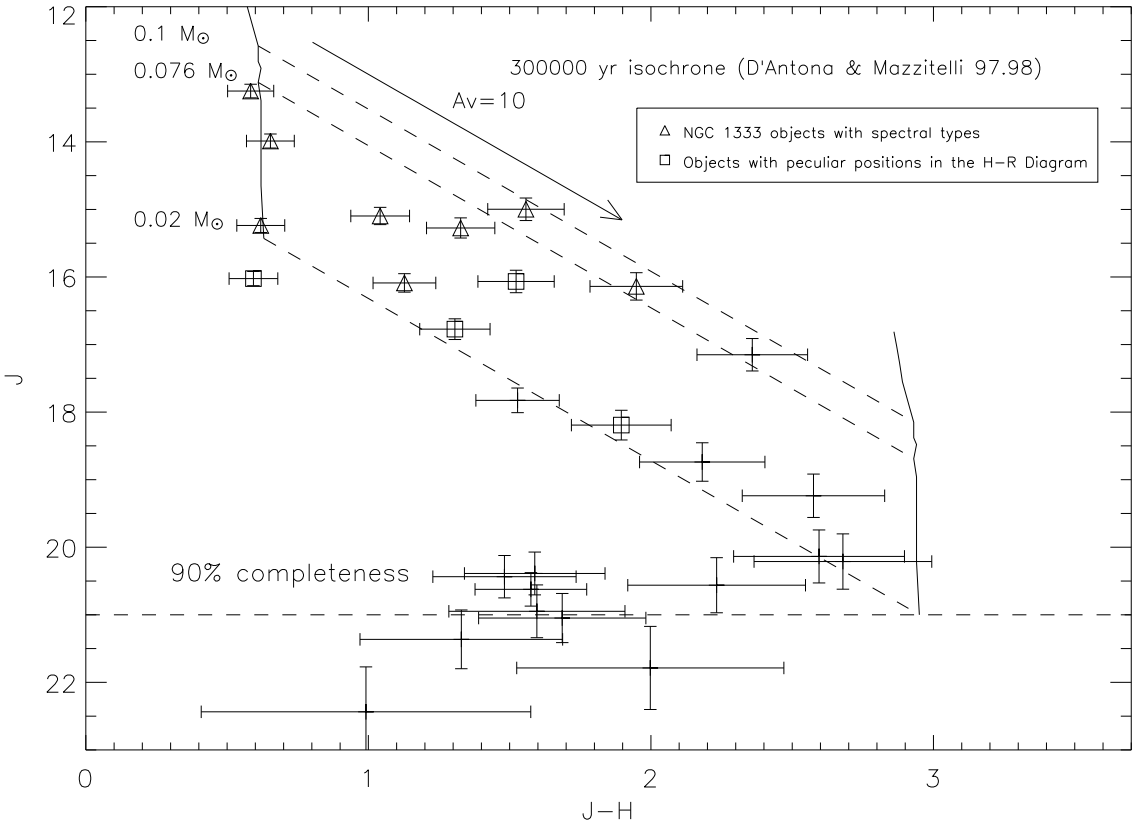

Fig. 6.— NICMOS photometry of sources detected in NGC 1333 transformed into the CIT system together with a 0.3 Myr (D'Antona & Mazzitelli 1997;1998) isochrone and the reddening vector also in the CIT system. The 90% completeness limit, derived from artificial star tests, is also shown. The objects with derived spectral types are marked.

Table 1. Log of Observations

Obs. Field	R.A. (J2000.0)	Dec. (J2000.0)	F110 exp. time	F160 exp. time
S1	03:28:56.41	+31:15:33.1	766s	383s
S2	03:29:03.16	+31:16:58.7	766s	383s
S3A	03:29:11.97	+31:16:58.2	766s	383s
S3B	03:29:12.38	+31:17:25.2	766s	383s
N2	03:29:11.65	+31:23:19.5	510s	256s
N7	03:29:04.1	+31:25:29.5	255s	128s
Roque 25	03:48:30.6	+22:44:50	256s	128s
Roque 33	03:48:49.0	+24:20:25	256s	128s
Teide 1	13:05:40.18	-25:41:06.0	256s	128s
J0205.5-1159	02:05:29.40	-11:59:29.7	256s	128s
Sigma Ori 60	05:39:37.62	-02:30:45.64	256s	128s
Sigma Ori 47/27	05:38:16.00	-02:40:23.80	256s	128s

Table 2. Photometry of sources detected in J- or H-band

Object ID	R.A. (J2000.0)	Dec. (J2000.0)	J	Jerr	H	Herr	ASR ID[a]	Notes
S1-1	03:28:54.938	+31:15:29.65	16.09	0.14	14.96	0.05	109	
S1-2	03:28:55.334	+31:15:53.83	N/A	N/A	20.00	0.23	N/A	
S1-3	03:28:56.020	+31:15:49.28	20.62	0.25	19.05	0.10	16	Possible Outflow
S1-4	03:28:56.959	+31:15:50.93	15.10	0.13	14.06	0.04	15	
S1-5	03:28:57.162	+31:15:35.19	15.28	0.15	13.95	0.05	17	
S1-6	03:28:57.388	+31:15:36.72	17.83	0.18	16.30	0.07	N/A	
S1-7	03:28:57.990	+31:15:50.36	N/A	N/A	21.03	0.39	N/A	
S1-8	03:28:58.058	+31:15:48.65	19.24	0.32	16.67	0.10	N/A	
S2-1	03:29:01.673	+31:17:12.25	20.44	0.31	18.96	0.16	N/A	
S2-2	03:29:01.876	+31:16:43.98	21.79	0.62	19.79	0.24	N/A	
S2-3	03:29:01.929	+31:16:53.22	16.77	0.15	15.47	0.06	11	
S2-4	03:29:02.654	+31:17:14.84	22.44	0.66	21.45	0.48	N/A	
S2-5	03:29:04.077	+31:16:59.71	20.95	0.39	19.36	0.19	N/A	
S2-6	03:29:04.114	+31:17:07.46	13.25	0.10	12.67	0.03	8	
S2-7	03:29:04.179	+31:16:50.93	18.74	0.28	16.56	0.09	9b	
S2-8	03:29:04.229	+31:16:50.60	17.15	0.24	14.80	0.09	9a	
S2-9	03:29:04.713	+31:16:59.03	15.00	0.17	13.44	0.06	105	
S2-10	03:29:05.413	+31:17:02.57	20.56	0.41	18.33	0.14	N/A	
S3B-6	03:29:10.716	+31:17:21.34	21.36	0.44	20.04	0.25	N/A	
S3A-1	03:29:10.787	+31:16:43.99	16.07	0.17	14.55	0.06	23	
S3A-2	03:29:11.272	+31:17:18.85	13.95	0.10	13.30	0.04	24	Both in frame S3A & S3B
S3B-3	03:29:11.353	+31:17:17.52	13.99	0.09	13.31	0.03	24	Both in frame S3A & S3B
S3A-3	03:29:12.923	+31:17:08.34	15.94	0.11	15.38	0.04	25	Both in frame S3A & S3B

Table 2—Continued

Object ID	R.A. (J2000.0)	Dec. (J2000.0)	J	Jerr	H	Herr	ASR ID[a]	Notes
S3B-4	03:29:13.008	+31:17:07.01	16.02	0.15	15.40	0.04	25	Both in frame S3A & S3B
S3A-4	03:29:13.014	+31:16:41.12	18.19	0.22	16.30	0.08	26	
S3B-7	03:29:13.034	+31:17:37.34	20.39	0.32	18.80	0.13	28b	
S3B-1	03:29:13.078	+31:17:38.24	15.24	0.10	14.62	0.04	28a	
S3A-5	03:29:13.269	+31:17:17.35	20.21	0.41	17.54	0.12	27	Both in frame S3A & S3B
S3A-6	03:29:13.283	+31:16:45.91	23.37	2.38	19.47	0.37	N/A	
S3B-5	03:29:13.351	+31:17:16.01	20.14	0.39	17.55	0.12	27	Both in frame S3A & S3B
S3B-2	03:29:13.655	+31:17:43.48	16.14	0.20	14.19	0.07	29	
S3A-7	03:29:14.285	+31:17:00.58	21.05	0.36	19.37	0.19	N/A	

[a]ASR refers to Aspin et al. (1994)

Table 3. Spectral Standards

ID	R.A. (J2000.0)	Dec. (J2000.0)	Spectral Type[a]	Q[b]	Prop ID
GL 328	08:55:07.62	+01:32:47.4	M0	0.87	7322
GL 908	23:49:12.53	+02:24:04.4	M1	0.98	7830
GJ 623	16:24:09.32	+48:21:10.5	M2.5	1.25 ± 0.01	7322
GL 388	10:19:36.50	+19:52:10.6	M3	1.38	7322
GL 569a	15:43:02.12	+26:16:36.0	M3	1.50	7322
GJ 748	16:24:09.32	+48:21:10.5	M3.5	1.15	7830
GL 896a	23:31:52.18	+19:56:14.1	M3.5	1.46	7830
GL 213	05:42:09.27	+12:29:21.6	M4	1.56	7322
GJ 699	17:57:48.50	+04:41:36.2	M4	1.16 ± 0.01	7322
GJ 473a	12:33:16.3	+09:01:26	M4	1.26	7830
GL 83.1	16:36:21.45	-02:19:28.5	M4.5	1.56	7322
GJ 1245a	19:53:54.48	+44:24:53.3	M5.5	1.23 ± 0.01	7830
GL 406	10:56:28.99	+07:00:52.0	M6	1.16 ± 0.02	7322
GJ 1111	08:29:49.35	+26:46:33.7	M6.5	1.59	7322
GJ 473b	12:33:19.1	+09:01:10	M7	1.67 ± 0.01	7830
LHS 3003	14:56:38.31	-28:09:47.4	M7	2.03	7322
VB 8	16:55:35.29	-08:23:40.1	M7	1.68	7322
VB 10	19:16:57.66	+05:09:00.4	M8	2.10	7322
Teide 1	13:05:40.18	-25:41:06.0	M8	1.69 ± 0.03	9846
GL 569b	15:43:03.8	+26:15:59	M8.5	2.29	7322
LHS 2924	14:28:43.33	+33:10:37.9	M9	2.42	7322
Roque 33	03:48:49.0	+24:20:25	L0	1.52 ± 0.06	9846
Roque 25	03:48:30.6	+22:44:50	L0	2.16 ± 0.22	9846
Kelu 1	13:05:40.18	-25:41:06.0	L2	2.79	7830
J1228-1547	12:28:15.23	-15:47:34.2	L5	3.51	7830
J0205.5-1159	02:05:29.40	-11:59:29.7	L7	3.71 ± 0.22	9846

[a]Spectral Types are from Kirkpatrick et al. (1991), Henry et al. (1994), Martìn et al. (2000) and Kirkpatrick et al. (1999)

[b]Errors for Q are only given for objects with 4 or more spectra

Table 4. Properties of NGC 1333 objects with spectral types

Object Name[a]	Spectral Type	Log(Teff)[b]	J-H[c]	H-K	K	A_v[d]	Log($L/L_\odot$)[e]	r_k[f]	Q	Notes[g]
ASR24	M8 ± 0.8	3.38	0.60	0.42	12.94	0.0	-1.52	0.02	2.02 ± 0.05	M8.2
ASR25	M4 ± 0.6	3.51	0.70	0.70	15.33	0.7	-2.31	0.42	1.36 ± 0.09	
ASR29	M5 ± 0.8	3.46	2.08	1.16	13.05	13.7	-1.02	-0.04	1.57 ± 0.07	
ASR109	M8 ± 0.8	3.40	1.01	0.67	13.24	3.6	-1.92	-0.01	1.93 ± 0.05	
ASR11	M4 ± 0.6	3.50	1.15	0.58	14.89	4.8	-2.05	0.00	1.27 ± 0.02	
ASR105	M6 ± 0.8	3.45	1.56	1.19	12.69	8.5	-1.21	0.29	1.62 ± 0.07	
ASR17	M6 ± 0.7	3.44	1.36	0.75	13.21	4.8	-1.37	0.08	1.67 ± 0.02	M7.4
ASR26	<M0 ± 0.7	3.58	1.59	0.85	15.54	8.8	-1.83	0.18	0.90 ± 0.01	
ASR8	M7 ± 1.1	3.43	0.63	0.33	12.34	0.1	-1.26	-0.07	1.76 ± 0.17	
ASR28	M7 ± 0.8	3.41	0.64	0.39	14.18	0.2	-2.00	-0.02	1.89 ± 0.05	Binary
ASR15	M6 ± 0.7	3.44	0.99	0.53	13.49	3.3	-1.60	-0.04	1.66 ± 0.03	M7.4
ASR23	<M0 ± 0.6	3.58	1.48	0.76	13.33	7.8	-1.04	0.16	0.89 ± 0.07	
MBO20	M3 ± 0.6	3.51	1.75	0.88	10.91	10.9	-0.17	-0.05	1.19 ± 0.02	
MBO78	M5 ± 0.7	3.47	1.78	1.18	13.37	10.8	-1.35	0.16	1.45 ± 0.05	

[a]ASR designations are from Aspin et al. (1994); MBO designations are from Wilking et al. (2004)

[b]Typical errors are ≈ 0.1

[c]2MASS photometry for the objects listed. This was used to derive r_k.

[d]Typical errors are ≈ 1

[e]Typical errors are ≈ 0.15

[f]Typical errors are ≈ 0.1

[g]Spectral types derived by Wilking et al. (2004)

Table 5. Ratios of intermediate-mass stars to low-mass objects

Region	N(0.1-1 $M_\odot$)/N(0.03 - 0.1 $M_\odot$)
Pleiades[a]	3.3 +2.2/-1.0
Chamaeleon[b]	5.6 +2.4/-4.5
Mon R2[c]	5.3 ± 3.35
Taurus[d]	4.0 ± 1.2
IC 348[e]	3.0 ± 0.5
Orion[f]	3.3 ± 0.6
NGC 1333	$R_1 = 0.14 \pm 0.047$
NGC 1333	$R_2 = 0.64 \pm 0.38$

[a]Data from Moraux et al. (2003)

[b]Data from Luhman (2004a)

[c]Data from Andersen et al. (2006)

[d]Data from Luhman (2004b)

[e]Data from Luhman et al. (2003a)

[f]Data from Hillenbrand & Carpenter (2000)